



# Effect of Ag on High-Temperature Oxidation Behavior of Mg–6.5Gd–5.6Y–0.1Nd–0.01Ce–0.4Zr Alloy

Shuang Guo<sup>1,2</sup> · Tianyu Liu<sup>2,3</sup> · Tianjiao Luo<sup>2,3</sup> · Yingju Li<sup>2,3</sup> · Xiaohui Feng<sup>2,3</sup> · Qiuyan Huang<sup>2,3</sup> · Ce Zheng<sup>2,3</sup> · Cheng Zhu<sup>2,3</sup> · Yuansheng Yang<sup>2,3,4</sup> · Weirong Li<sup>5</sup> · Feng Li<sup>1</sup>

Received: 12 February 2024 / Revised: 22 March 2024 / Accepted: 3 April 2024  
© The Chinese Society for Metals (CSM) and Springer-Verlag GmbH Germany, part of Springer Nature 2024

## Abstract

In this paper, the isothermal oxidation experiments were used to study the effect of Ag on the high-temperature oxidation behavior of Mg–6.5Gd–5.6Y–0.1Nd–0.01Ce–0.4Zr (wt%) alloy oxidized at 350 °C, 400 °C and 450 °C for 120 h. The results show that the oxidation weight gain of the alloy mainly occurs in the early oxidation stage (0–20 h). This reason attributes to the lack of protective oxide film and the rapid inward diffusion of oxygen through the macroscopic defects of the incomplete oxide film. When dense oxide films such as Y<sub>2</sub>O<sub>3</sub>, Gd<sub>2</sub>O<sub>3</sub>, and ZrO<sub>2</sub> form, they hinder the inward transport of oxygen ions and improve the high-temperature oxidation resistance of the alloy. In addition, the role of the Ag element at three temperatures is different. The addition of Ag mainly promotes the formation of eutectic phases such as Mg<sub>3</sub>Gd, Mg<sub>24</sub>Y<sub>5</sub>, and Ag<sub>2</sub>Gd, which reduces the content of Gd and Y elements in the alloy matrix, resulting in a decrease in the diffusion rate of Gd and Y elements during the oxidation process at 350 °C and 400 °C, and weakens the oxidation resistance of Ag-containing alloys. However, in the oxidation experiment at 450 °C, a large amount of eutectic phase is solid dissolved into the matrix, reducing the difference in element content. At this time, it is detected that the Ag element promoted the outward diffusion of Gd and Y elements, accelerating the formation of the oxide film. The oxidation resistance of Ag-containing alloys is improved.

**Keywords** Magnesium alloy · High-temperature oxidation · Thermogravimetric analysis · Gibbs free energy · Oxide film · Oxidation resistance

## 1 Introduction

Magnesium alloy has good mechanical properties. Due to its low density and high specific strength, it can significantly reduce the weight of components. It is known as a green, environmentally friendly, and ecological structural metal material in the twenty-first century. It is especially suitable for lightweight structural parts and has recently been used in aviation. Aerospace, automotive, and electronics applications have made significant progress [1–6]. However, magnesium alloys have poor high-temperature resistance, significantly limiting their applications. Currently, many research studies focus on improving the high-temperature properties of magnesium alloys. Research shows that alloying is a crucial method to improve the heat resistance of magnesium alloys [7–9]. Adding rare earth elements to magnesium alloys can improve room temperature and high-temperature properties, especially Mg–Gd–Y alloys represented by Gd and Y elements. Gd and Y have significant solid solubility in magnesium alloys, can form effective strengthening phases,

Available online at <http://link.springer.com/journal/40195>.

✉ Tianjiao Luo  
tjluo@imr.ac.cn

✉ Feng Li  
lifhr@sut.edu.cn

- <sup>1</sup> School of Materials Science and Engineering, Shenyang University of Technology, Shenyang 110870, China
- <sup>2</sup> Institute of Metal Research, Chinese Academy of Science, Shenyang 110016, China
- <sup>3</sup> School of Materials Science and Engineering, University of Science and Technology of China, Hefei 230026, China
- <sup>4</sup> Shandong Provincial Key Laboratory of High Strength Lightweight Metallic Materials, Qilu University of Technology (Shandong Academy of Sciences), Jinan 250014, China
- <sup>5</sup> Dongguan EONTEC Co. Ltd, Guangdong 523662, China

and have significant age-hardening effects, potentially improve the heat resistance of magnesium alloys [10–12]. Moreover, Gd and Y elements can form a dense oxide film at high temperature to improve the oxidation resistance of the alloy, which has great potential to improve the heat resistance of magnesium alloys. But adding excessive Gd can lead to increased costs and decreased ductility, so other elements need to be used to solve these problems. Zr can refine grains, improve microstructure uniformity and reduce hot cracking tendency in magnesium alloys without Al, while Nd and Ce can refine grains, so that magnesium alloys with good thermal stability and excellent high-temperature performance can be obtained. On this basis, Mg–6.5Gd–5.6Y–0.1Nd–0.01Ce–0.4Zr (wt%) alloy was selected in this study, and the experimental results show that the alloy has excellent high-temperature properties.

In addition, through previous experimental results and literature research, it was found that the Ag element played a positive role in promoting dynamic recrystallization and grain refinement [13]. Researches show that Ag can accelerate the age-hardening response of the alloys, form a large number of  $\beta'$  and  $\gamma''$  phases in the alloys, significantly improve the room temperature and high-temperature properties of the magnesium alloys [14–17]. Wang et al. [18] used ordinary casting processes and heat treatment processes to develop ultra-high-strength Mg–8.5Gd–2.3Y–1.8Ag–0.4Zr alloy with good ductility. After solution treatment at 500 °C for 10 h and aging at 200 °C for 32 h, the room temperature yield strength, tensile strength, and elongation of the cast T6 alloy were 268 MPa, 403 MPa, and 4.9%, respectively.

Adding Ag can improve solid solution strengthening and enhance the age-hardening reaction. The enhanced age-hardening response attributes to underlying nanoscale platelet precipitates (not observed in Ag-free alloys) and the refinement of  $\beta'$  phase. The co-precipitation strengthening effect produced by  $\beta'$  phase and plate-like precipitates is considered the most significant contributor to the strength of cast T6 alloy. Zhang et al. [19] used atom probe tomography (APT) technology to detect Ag-rich clusters in Mg–Gd–Ag–Zr alloy after solution treatment and water quenching. A high-density essential precipitation phase was observed in the early stage of subsequent isothermal aging at 200 °C, proving that adding Ag to the age-hardening Mg–Gd–Zr alloy system can significantly enhance early age-hardening kinetics. Najafi et al. [20] studied the effects of adding 0.5 wt%, 1 wt%, and 1.5 wt% Ag on the microstructural evolution, thermal stability, and mechanical properties of Mg–5Gd–1Y (GW51) alloy. The results showed that the addition of Ag refined the dendrite structure of the matrix alloy, promoted the formation of a new  $\text{Mg}_6\text{Gd}_2\text{YAg}$  phase, and increased the volume fraction of  $\text{Mg}_5(\text{Gd}, \text{Y})$  particles. These effects result in

improved hardness, strength, and microstructural stability of Ag-containing alloys both as cast and after long-term exposure to high temperatures.

However, high-temperature oxidation is a common form of failure for metal materials and a crucial problem during service of the component [21]. Magnesium alloys can undergo high-temperature oxidation under high-temperature conditions. Therefore, research on the oxidation resistance of magnesium alloys is also vital. Previous studies have shown that Ag can effectively improve the high-temperature stability of the microstructure of magnesium alloys. However, there are few reports about the effect of Ag element on the oxidation behavior of magnesium alloys at high temperature. Therefore, we study the effect of Ag element on the high-temperature oxidation behavior of Mg–6.5Gd–5.6Y–0.1Nd–0.01Ce–0.4Zr alloy and analyze its mechanism.

## 2 Experimental

### 2.1 Alloys Preparation

In the experiment, Mg was added in the form of industrial pure magnesium with a purity of 99.6 wt%, alloy elements Gd, Y, Nd, Zr, and Ag were added in the form of Mg–30 wt% Gd, Mg–30 wt% Y, Mg–30 wt% Nd, Mg–30 wt% Zr, Mg–25 wt% Ce intermediate alloys, and Ag was added in the form of 99.99 wt% pure silver. The oxide scale on the surface of the raw materials was polished to ensure their purity. Before smelting, all materials were put into a drying oven to prevent magnesium from reacting with water vapor during the smelting process, which could quickly produce holes. The alloy was prepared in a well-type resistance melting furnace. Put pure magnesium into the crucible. The furnace temperature was raised to 750 °C to melt the alloy. After standing for 20 min, the surface oxide scale and impurities were removed, and Mg–30%Gd, Mg–30%Nd, Mg–25%Ce, and Ag were added; then, the temperature raised to 780 °C, and Mg–30%Zr, Mg–30%Y alloys were added, stirred evenly, and immediately poured into a preheated mold at 250 °C. During the smelting and pouring process, a mixed gas of  $\text{CO}_2$  and  $\text{SF}_6$  with a volume ratio of 99:1 was used for protection, and four types of Mg–6.5Gd–5.6Y–0.1Nd–0.01Ce–0.4Zr magnesium alloys containing Ag were prepared.

### 2.2 Analysis Methods

The actual composition of the alloys used in the experiment is listed in Table 1. The four alloys were named 0Ag, 1.0Ag, 1.5Ag, and 2.0Ag, respectively. The size of the sample for the oxidation experiment was 20 mm × 10 mm × 1.5 mm. It was ground to 5000# with SiC sandpaper and then, polished

**Table 1** Actual composition of the alloy (wt%)

Samples	Gd	Y	Zr	Nd	Ce	Ag	Mg
0Ag	6.51	5.73	0.26	0.11	0.011	–	Bal.
1.0Ag	6.47	5.66	0.31	0.12	0.015	1.04	Bal.
1.5Ag	6.30	5.84	0.29	0.12	0.015	1.63	Bal.
2.0Ag	6.40	5.47	0.22	0.12	0.015	2.09	Bal.

for later use. In order to ensure the accuracy of the oxidation experiment data, three parallel samples of each alloy were tested, and the static weight gain method was used to conduct a constant temperature oxidation experiment. The experimental temperatures were 350 °C, 400 °C, and 450 °C, respectively. Pair the oxidized samples whose surface area had been cleaned and measured with an alumina crucible calcined to a constant weight, and weighed it in sequence, recorded the original mass (accurate to 0.01 mg). The oxidation experiment was carried out in a box-type resistance furnace. Before the experiment, the resistance furnace was preheated to the experimental temperature, and then, the crucible containing the sample was placed in the resistance furnace to start the experiment. After constant temperature oxidation for 1 h, 3 h, 5 h, 20 h, 40 h, 60 h, 80 h, and 120 h, respectively, the samples were taken out from the resistance furnace. After air cooling and weighing, the samples were put back into the resistance furnace. Repeat the above steps, until the total oxidation time reaches 120 h.

The alloy composition was analyzed by plasma spectrometer (OPTIMA7300DV), the AxioObserverZ1 metallographic microscope (OM), and the InspecF50 scanning electron microscope (SEM) equipped with an energy disperse spectroscopy (EDS) probe was used to observe the microstructure of the samples and analyze the precipitation phases. A Smart Lab X-ray diffractometer (XRD) was used to conduct physical phases analysis of the oxide film of the alloys, an Apreo scanning electron microscope (SEM) was used to observe the morphology of the alloys surface and cross-section oxide film, and EDS was used to analyze the element distribution of the oxide film.

## 3 Results

### 3.1 As-cast Alloys Structure

Figure 1 illustrates the as-cast microstructure of the four alloys. As shown in Fig. 1, the alloys structure consists of  $\alpha$ -Mg (point A) matrix, gray and a small amount of bright white precipitates. Figure 2 illustrates the XRD patterns of the four alloys. Combined with the EDS analysis data in Table 2, it can be seen that the gray precipitates are mainly composed of  $\text{Mg}_3\text{Gd}$  and  $\text{Mg}_{24}\text{Y}_5$  (point B) phases, and the bright white precipitates are mainly composed of  $\text{Ag}_2\text{Gd}$

phase (point E). When Ag is not added, the alloy has less precipitate content and a more dispersed distribution. With the addition of the Ag element, a new phase of  $\text{Ag}_2\text{Gd}$  is formed, and the eutectic phase in the alloys gradually grows and is distributed more continuously. This is because the gradual increase in Ag element can enrich more solute elements in front of the solid–liquid interface during solidification, leading to the growth and coarsening of eutectic. In addition, the cubic Y-rich phase (C point) and the flocculent Zr (D point) element-rich area were also found under the scanning electron microscope. These phases were not detected on XRD. Studies have shown that the cubic phase is generally considered to be a  $\text{REH}_2$  compound [22] or RE solid solution [23].

### 3.2 Oxidation Kinetic

To compare the oxidation resistance of 0Ag, 1.0Ag, 1.5Ag, and 2.0Ag alloys at high temperatures, Mg–6.5Gd–5.6Y–0.1Nd–0.01Ce–0.4Zr– $x$ Ag alloys were subjected to 120 h oxidation experiments at 350 °C, 400 °C, and 450 °C. Figure 3 illustrates the isothermal oxidation weight gain curves of four alloys at 350 °C, 400 °C, and 450 °C. Figure 3a and b, respectively, shows the oxidation weight gain curves of four alloys at 350 °C and 400 °C. During the oxidation process, all four curves contain two oxidation stages. In the first stage, the weight of the alloy increases rapidly, which mainly includes the absorption of O and the initial formation of the oxide film. The first stage lasts approximately 20 h. In the second stage, the oxidation weight gain of the four alloys shows a slowly increasing trend and gradually tends to stabilize. From the graph, it can be seen that the oxidation weight gain of Mg–6.5Gd–5.6Y–0.1Nd–0.01Ce–0.4Zr alloy with Ag added is higher than that of 0Ag alloy, but the oxidation weight gain of the four alloys is minimal. Figure 3c shows the oxidation weight gain curve of the four alloys at 450 °C, which shows significant changes compared to 350 °C and 400 °C. Although the four curves also contain two oxidation stages during the oxidation process at 450 °C.

Moreover, in the first stage, alloy oxidation weight gain increases rapidly, which mainly includes the absorption of O and the initial formation of the oxide film, but only lasts for 5 h. Compared to the two temperatures of 350 °C and 400 °C, the duration of the first stage is significantly reduced. In the

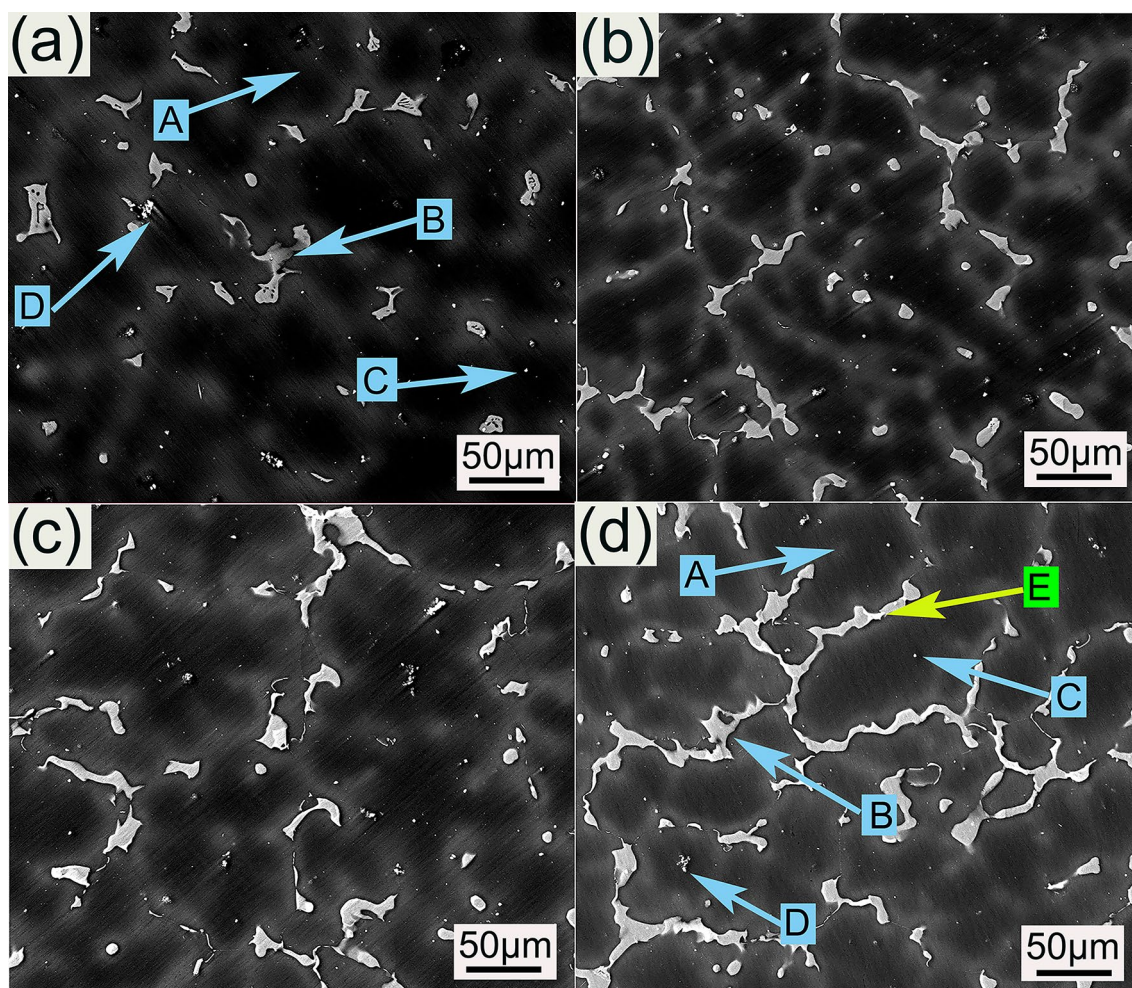


Fig. 1 Microstructure of as-cast alloys: a 0Ag, b 1.0Ag, c 1.5Ag, d 2.0Ag

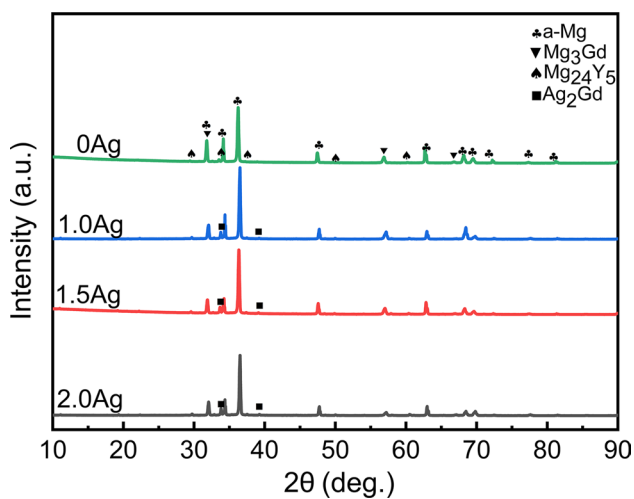


Fig. 2 XRD patterns of the as-cast alloys

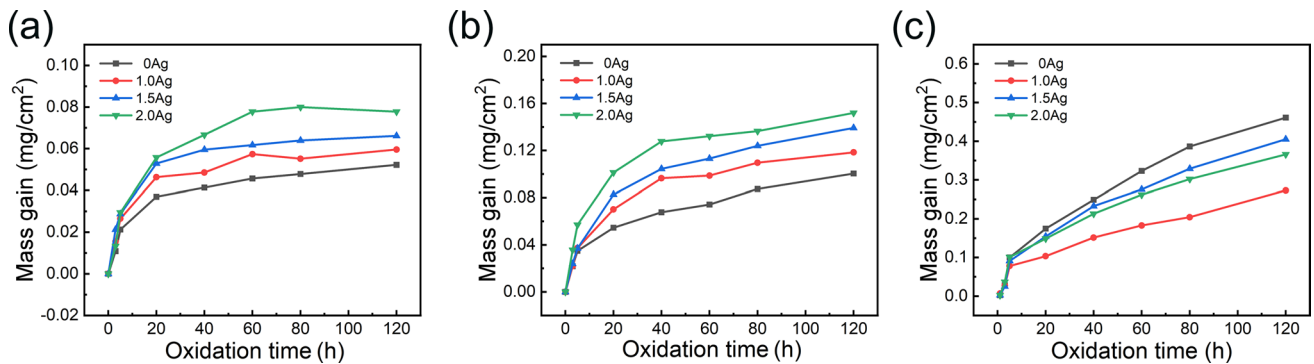
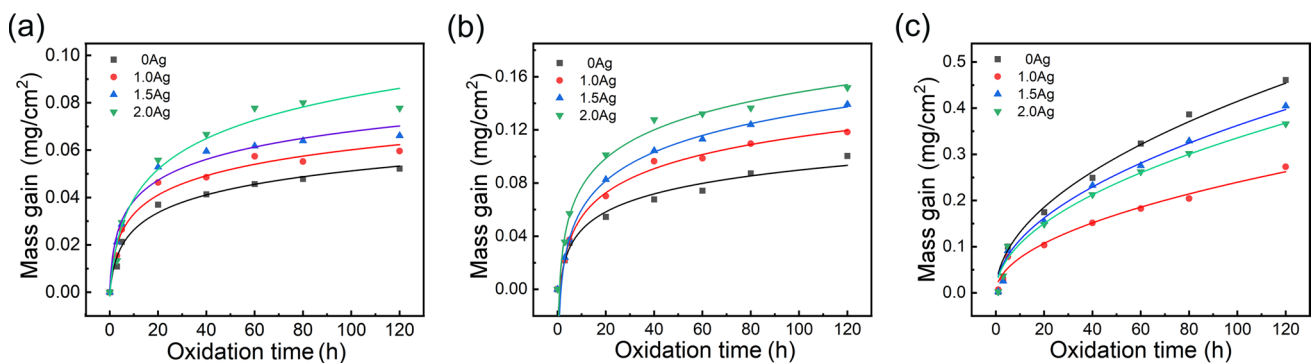
second stage, the oxidation weight gain trend of the four alloys slowed down. However, from the graph, it can be seen that the oxidation weight gain of Mg–6.5Gd–5.6Y–0.1Nd–0.01Ce–0.4 Zr alloy with Ag addition is lower than that of 0Ag alloy, and different changes occur in the oxidation weight gain of the alloy with the increase in Ag content. Among them, 0Ag alloy has the most significant oxidation weight gain, while 1.0Ag alloy has the smallest.

The oxidation rate constant of alloys can be calculated using formulas (1) and (2) [24], and the oxidation experimental data can be substituted into the formula for fitting. Figure 4 shows the fitting curves of the oxidation weight gain of four alloys. As shown in Fig. 4, the fitted curve is similar to the actual oxidation weight gain curve. In order to better determine the degree of fit, the relevant parameters of the fitted curve are analyzed.

$$\Delta m = k \ln(t + c_1) + c_2. \quad (1)$$

**Table 2** EDS data of 2.0Ag alloy (wt%)

Points	Mg	Gd	Y	Zr	Nd	Ce	Ag
A	95.26	1.51	2.53	0.00	0.00	0.00	0.70
B	56.40	23.59	15.24	0.28	0.92	0.00	3.57
C	29.38	13.68	55.28	1.29	0.00	0.00	0
D	48.69	11.55	11.67	24.79	0.19	0.00	3.11
E	59.75	30.17	6.99	0.15	0.57	0.00	2.37

**Fig. 3** Oxidation weight gain curves of four alloys: **a** 350 °C, **b** 400 °C, **c** 450 °C**Fig. 4** Fitting curves of oxidation weight gain at different temperatures: **a** 350 °C, **b** 400 °C, **c** 450 °C

$$(\Delta m)n = k't. \quad (2)$$

where  $\Delta m$ -weight gain per unit area,  $\text{mg}/\text{cm}^2$ ;  $k$ -logarithmic curve oxidation rate constant,  $\text{mg}^2/(\text{cm}^4 \cdot \text{h})$ ;  $k'$ -parabolic oxidation rate constant,  $\text{mg}^2/(\text{cm}^4 \cdot \text{h})$ ;  $n$ -the rate index of oxidation rate law;  $t$ -isothermal oxidation time, h.

Table 3 shows the relevant parameters of the fitted curves for four different alloys at different temperatures. According to Table 3, all  $R^2$  values are more significant than 0.96, indicating that the fitted curve is very consistent with the variation pattern of the actual oxidation weight gain curve.

Therefore, the actual oxidation rate of the alloy can be analyzed by fitting the curve. Compare the oxidation

rate constant  $k$  and  $k'$  after fitting the function ( $n=2$ ), it is found that during the oxidation process of the four alloys at 350 °C and 400 °C, the oxidation rate constant  $k$  value gradually increases as the Ag content gradually increases. The oxidation weight gain curves of alloys all follow the logarithmic curve law. During the oxidation process at 450 °C, the oxidation rate constant  $k'$  value of Ag-containing alloys is lower than that of 0Ag alloys, with the oxidation rate constant  $k'$  value of 1.0Ag alloy being the smallest. At this time, the oxidation weight gain curve of the alloy follows the law of a quadratic exponential function.

**Table 3** Relevant data of fitting curves for four alloys at 350 °C, 400 °C and 450 °C

Alloys	Parameters	350 °C	400 °C	450 °C
0Ag	$k$	0.01123	0.01955	0.04146
	$R^2$	0.98149	0.97764	0.9793
	$c_1$	1.00275	$-2.37847 \times 10^{-19}$	–
	$c_2$	$-6.14477 \times 10^{-4}$	$-2.92413 \times 10^{-4}$	–
	$n$	–	–	1.7366
1.0Ag	$k$	0.01207	0.02622	0.02395
	$R^2$	0.96863	0.99493	0.97732
	$c_1$	0.66043	$-5.90181 \times 10^{-19}$	–
	$c_2$	0.00446	-0.00596	–
	$n$	–	–	1.9203
1.5Ag	$k$	0.01295	0.03107	0.03625
	$R^2$	0.97539	0.99865	0.98089
	$c_1$	0.51521	$-1.17842 \times 10^{-18}$	–
	$c_2$	0.00814	-0.0114	–
	$n$	–	–	1.7805
2.0Ag	$k$	0.01972	0.03096	0.03356
	$R^2$	0.9648	0.99245	0.98192
	$c_1$	1.41663	$-2.2075 \times 10^{-20}$	–
	$c_2$	-0.00857	0.00579	–
	$n$	–	–	1.9368

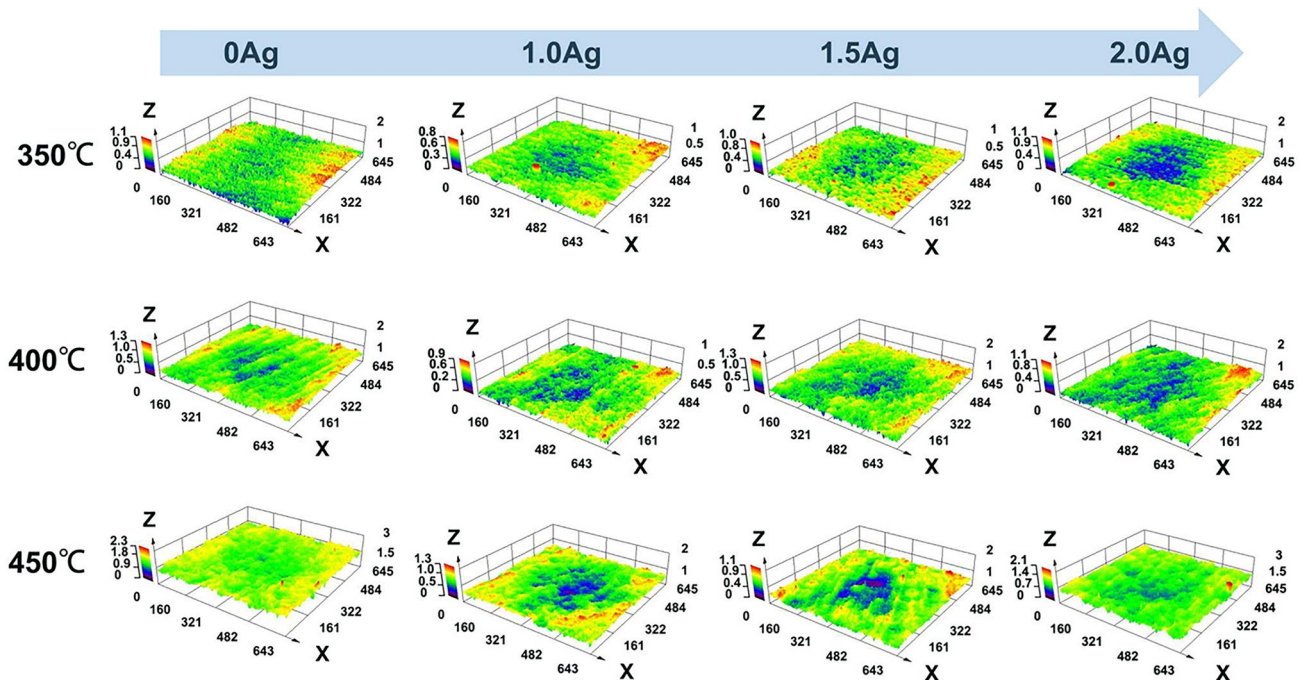
### 3.3 Morphology and Phase Analysis of Oxide Film

In order to facilitate the observation and analysis of the high-temperature oxide film morphology of the four alloys, the oxide samples were placed under laser confocal microscopy and scanning electron microscopy for observation. Figure 5 illustrates the three-dimensional morphology of the oxide film.

As shown in Fig. 5, the oxide film of the alloy is relatively flat. It has good anti-stripping properties at different temperatures, indicating that the four alloys have excellent oxidation resistance within this temperature range.

Figure 6 shows the surface oxidation morphology of four alloys under scanning electron microscopy. As shown in Fig. 6, the surface morphology of alloys with different Ag contents is almost the same at the same temperature. From the surface oxidation morphology at 350 °C and 400 °C, the oxide film is fragile and can be observed to cover the eutectic structure. As the temperature increases to 450 °C, the oxide film thickens and completely covers the substrate and eutectic phase. At this time, the film layer is very uniform and dense; this indicates that within this temperature range, the oxide films of different Ag-containing alloys are very intact and provide good protection to the substrate. The differences in the morphology of the oxide surface mainly come from temperature changes, and as the temperature increases, the oxide film gradually thickens.

Figure 7 shows the XRD patterns of four alloys after 120 h of oxidation at 350 °C, 400 °C, and 450 °C. As

**Fig. 5** Three-dimensional morphology of surface oxide films on four alloys at different temperatures for 120 h

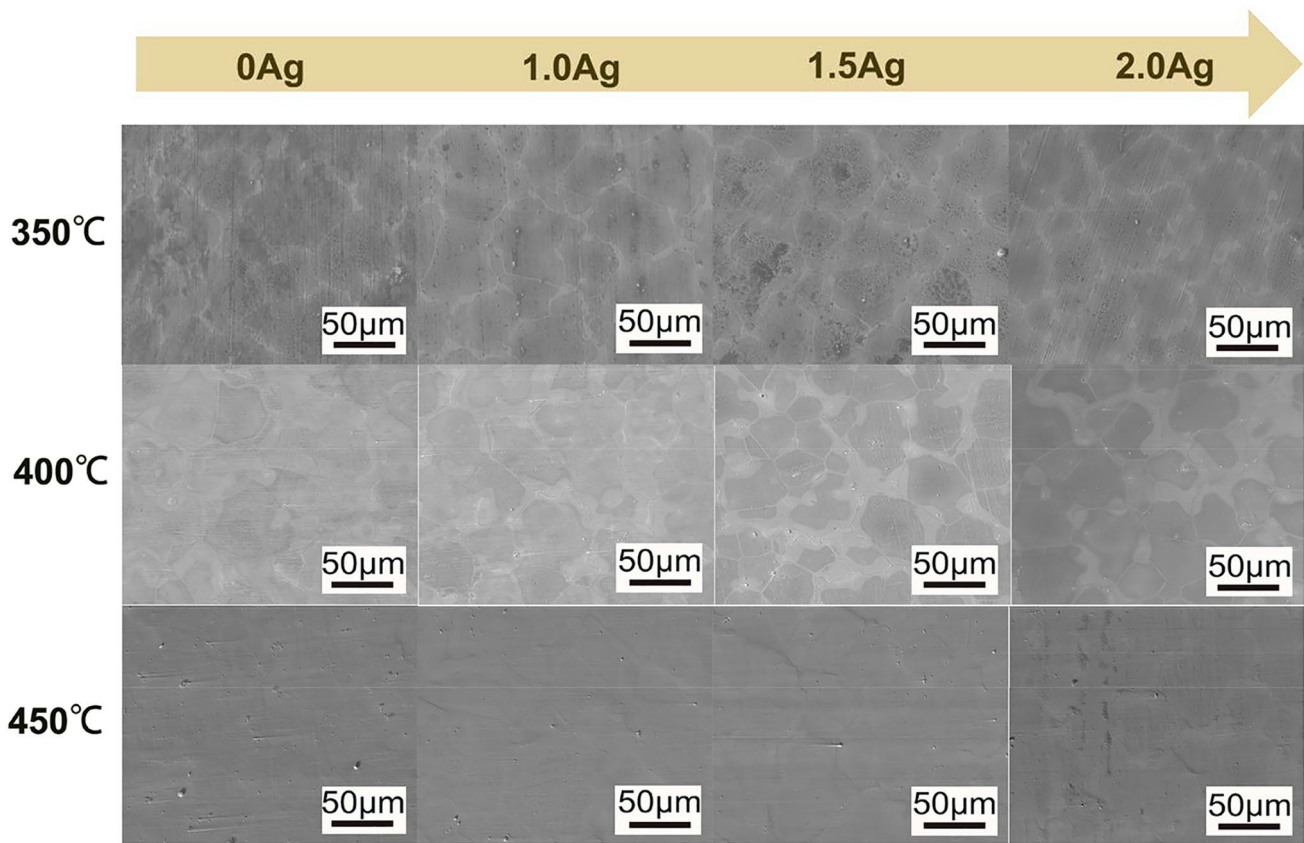


Fig. 6 Surface morphologies of four alloys oxidized at different temperatures for 120 h

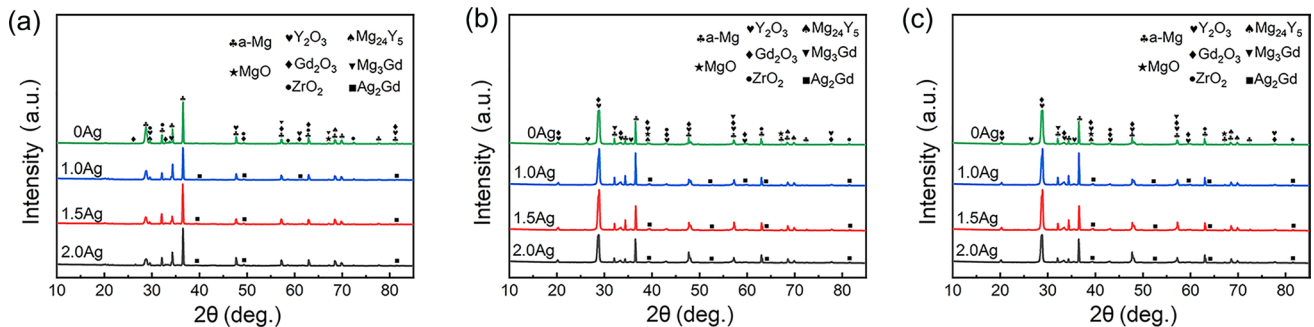
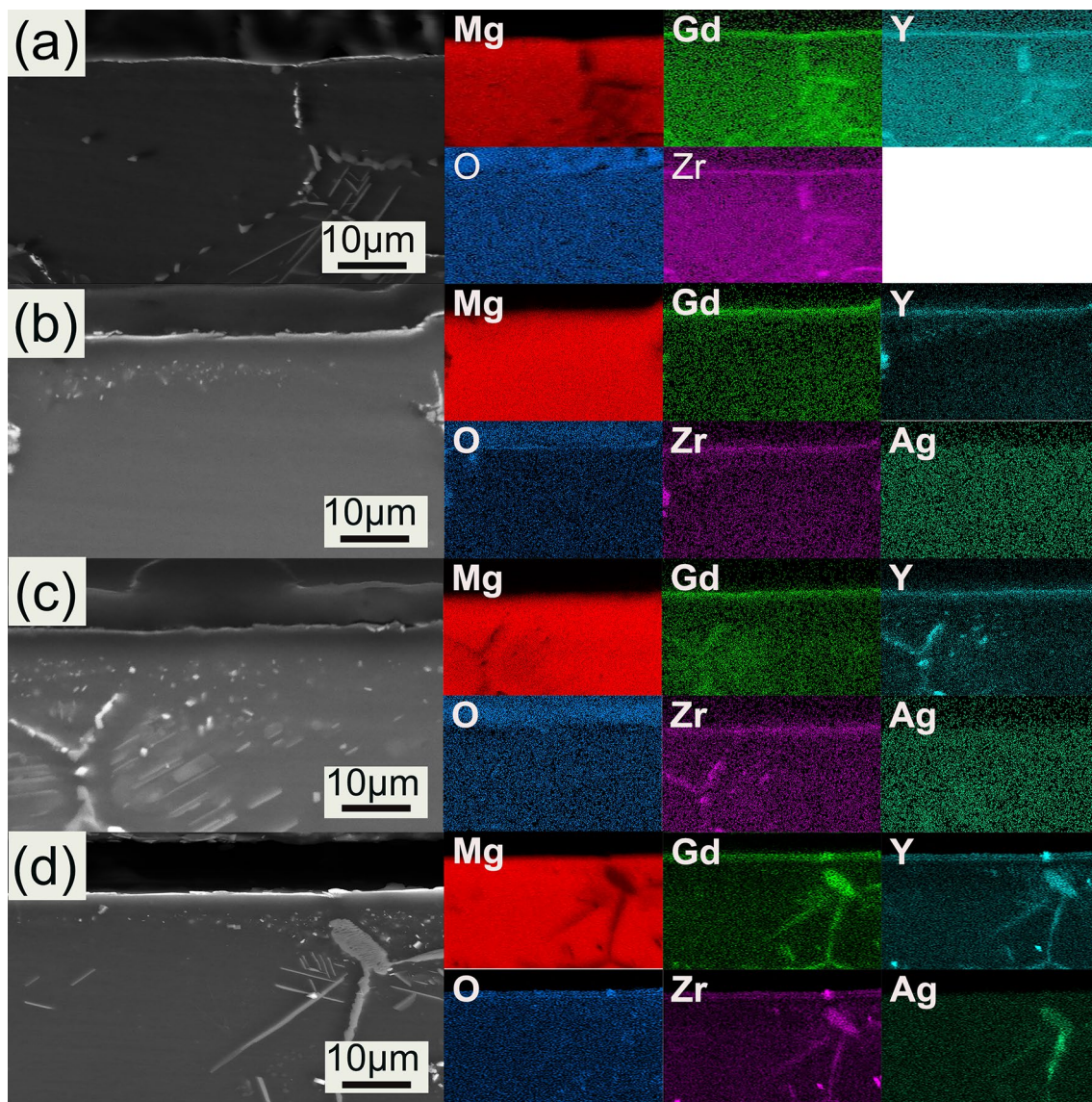


Fig. 7 XRD patterns of four alloys after oxidation for 120 h at different temperatures: **a** 350 °C, **b** 400 °C, **c** 450 °C

shown in Fig. 7, it can be seen that  $\text{Mg}_3\text{Gd}$ ,  $\text{Mg}_{24}\text{Y}_5$ , and  $\text{Ag}_2\text{Gd}$  eutectic phases are detected on the surface of the alloy after 120 h of oxidation at 350 °C, 400 °C, and 450 °C. In addition,  $\text{MgO}$ ,  $\text{Y}_2\text{O}_3$ ,  $\text{Gd}_2\text{O}_3$ , and  $\text{ZrO}_2$  were detected at different temperatures, indicating that the oxide film is mainly composed of these four oxides.

### 3.4 Cross-section Morphology and Element Distribution of Oxide Film

In order to test the oxide film thickness of the four alloys at different temperatures and observe their element distribution, the cross-sectional structure of the oxidized



**Fig. 8** Cross-section morphologies and element distribution of four alloys oxidized at 350 °C for 120 h: **a** 0Ag, **b** 1.0Ag, **c** 1.5Ag, **d** 2.0Ag

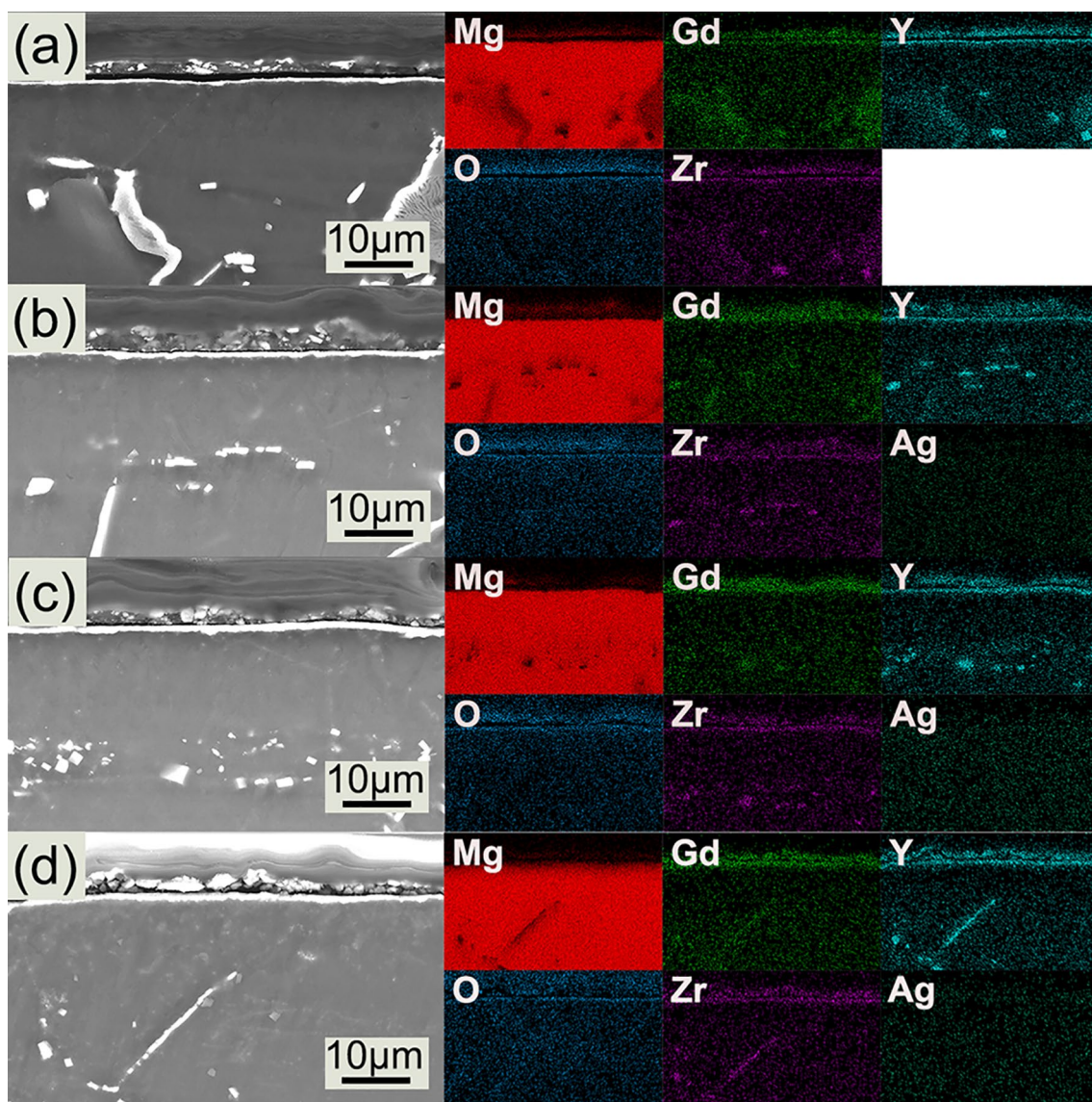
samples was placed under a scanning electron microscope for observation. Figure 8 shows the cross-sectional morphology of the oxide films of the four alloys after oxidation at 350 °C for 120 h. As shown in Fig. 8, the oxide film is thin and continuously distributed with a thickness of about 0.24–0.41 μm; its main components are Mg, Gd, Y, O, and Zr elements, consistent with the XRD detection results. A large amount of eutectic phase can be observed at this temperature, the main components of which are Gd, Y, and Zr elements, indicating that the proportion of eutectic phase under this condition is similar to that of the as-cast structure before oxidation without significant reduction.

Figure 9 shows the cross-sectional morphology of the oxide films of the four alloys after oxidation at 400 °C for 120 h. As shown in Fig. 9, the oxide films are very smooth

and continuously distributed, and the thickness of the oxide films has increased with an average thickness of about 0.73–0.97 μm; its main components are Mg, Gd, Y, O, and Zr elements, which is consistent with the XRD detection results. The composition of the oxide film does not change as the temperature changes, and a small amount of eutectic phase is dissolved, which can cause the Gd and Y content in the alloy matrix to increase.

Figure 10 shows the cross-sectional morphology of the oxide films of the four alloys after oxidation at 450 °C for 120 h. As shown in Fig. 10, the oxide films are smooth and continuously distributed. The thickness of the oxide films continues to increase, with an average thickness of about 1.05–1.38 μm; its main components are Mg, Gd, Y, O, and Zr elements, which is consistent with the XRD detection





**Fig. 9** Cross-section morphologies and element distribution of four alloys oxidized at 400 °C for 120 h: **a** 0Ag, **b** 1.0Ag, **c** 1.5Ag, **d** 2.0Ag

results. According to the cross-sectional morphology of the alloys, it can be seen that compared with the as-cast alloy structure, the number of eutectic phases in the oxidized alloy is significantly reduced. At this time, a large amount of solid solution has occurred in the eutectic phase, which can lead to an increase in the content of Gd and Y elements in the alloy matrix at this temperature. The content of elements in the four alloy matrices depends on their degree of phase solubility.

By comparing the cross-sectional structures of different Ag-containing alloys oxidized at 350 °C, 400 °C, and 450 °C, it was found that the compositions of the oxide films are all  $Y_2O_3$ ,  $Gd_2O_3$ ,  $ZrO_2$ , and a small amount of  $MgO$ , but no apparent stratification of the oxide films can be observed, indicating that the oxidized film layer is a composite film

structure. Moreover, the dissolution of the eutectic phase is very different, which can cause changes in the element content in the alloy matrix and affect the diffusion rate of elements. As the oxidation temperature increases, the oxide film can gradually thicken. The element content in the matrix can play a key role in resisting oxidation at higher temperatures.

#### 4 Discussion

Experimental results showed that adding Ag element has different effects on the high-temperature oxidation behavior of the alloy at different temperatures. In the oxidation experiments at 350 °C and 400 °C, adding Ag element

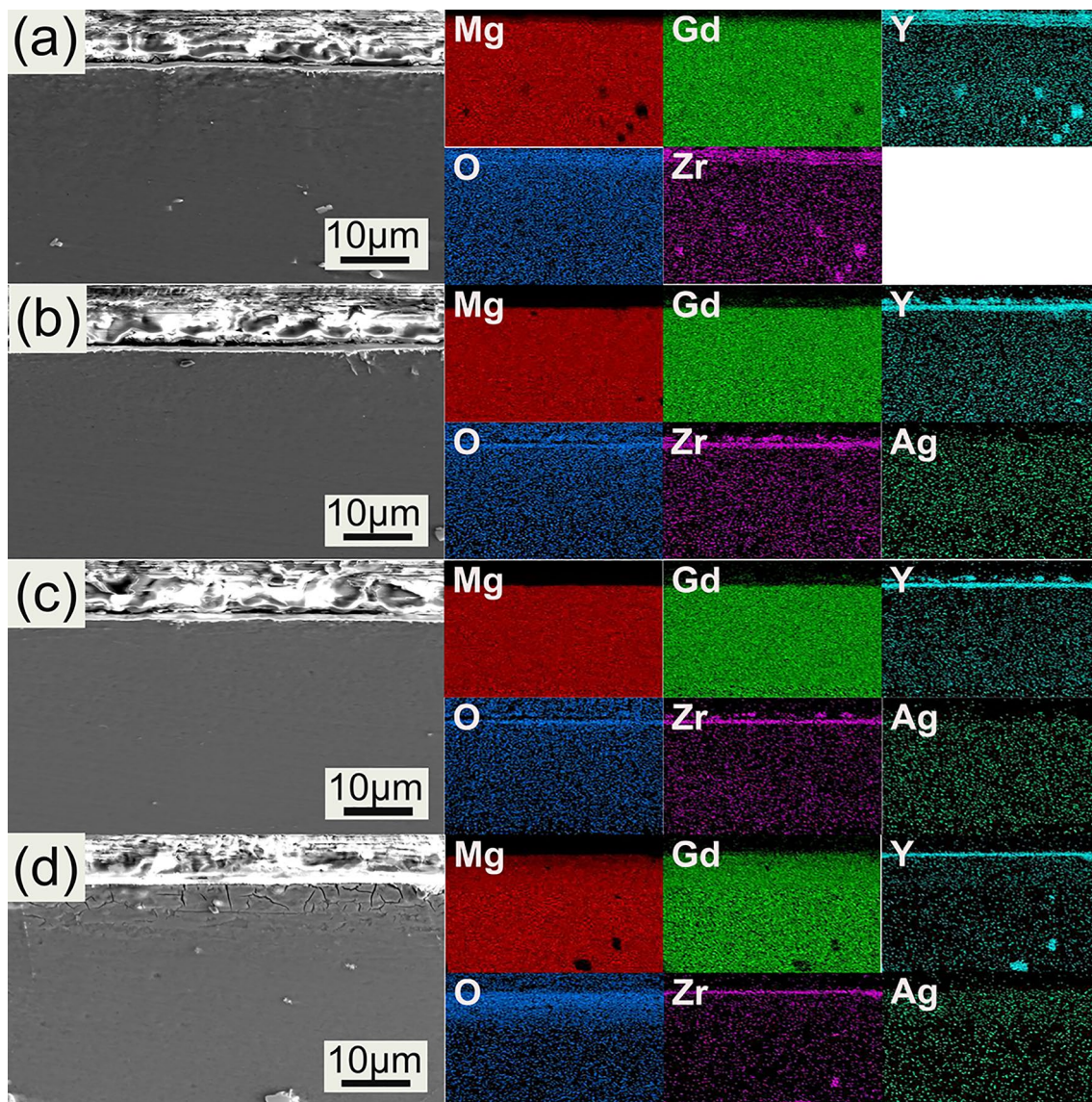


**Fig. 10** Cross-sectional morphologies and element distribution of four alloys after oxidation at 450 °C for 120 h: **a** 0Ag, **b** 1.0Ag, **c** 1.5Ag, **d** 2.0Ag

could increase the oxidation rate of the alloy, resulting in the weakening of the alloy's anti-oxidation performance. In the oxidation experiment at 450 °C, adding Ag element could reduce the oxidation rate and improve the oxidation resistance of the alloy. The analysis results of the influence of Ag element on the alloy oxidation mechanism were as follows.

#### 4.1 Oxidation Mechanism of Mg–6.5Gd–5.6Y–0.1Nd–0.01Ce–0.4Zr–*x*Ag Alloy

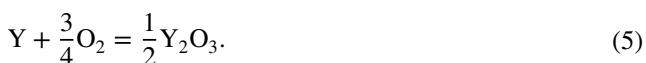
The Mg–6.5Gd–5.6Y–0.1Nd–0.01Ce–0.4Zr–*x*Ag alloys undergo complex oxidation processes at different temperatures. As shown in Fig. 4, after the oxide film forms in the early

high-temperature oxidation process, the oxidation weight gain rate at 350 °C and 400 °C gradually decreases with time extending up to 20 h. In comparison, the oxidation weight gain rate at 450 °C starts after only 5 h. Relevant studies have shown that the weight gain of the samples mainly occurred in the initial stage. This result was attributed to the lack of a protective oxide scale and the rapid inward transmission of oxygen through the macroscopic defects of the discontinuous oxide scale [25]. Further analysis of the oxide's volume ratio (PBR) to the corresponding pure metal shows that when the PBR of the oxide is between 1 and 2, the oxide film on the alloy surface is complete, dense, protective and has strong oxidation resistance. When the PBR value is less than 1, the oxide film on the alloy surface is affected by tensile stress,

resulting in a loose and porous oxide film with poor resistance to oxygen erosion forms [26]. The alloy matrix element in this article is Mg, which has active chemical properties and a high affinity with O. After oxidation begins, it quickly reacts with oxygen to form MgO. The PBR of MgO is 0.81 (less than 1). According to the above theory, the MgO oxide film on the surface of the alloy provides limited oxidation resistance to the alloy.

Furthermore, the alloy also formed oxide films such as Gd<sub>2</sub>O<sub>3</sub>, Y<sub>2</sub>O<sub>3</sub>, and ZrO<sub>2</sub> during the oxidation process. The PBR values of these oxidation products are 1.23, 1.39, and 1.56, which were all greater than 1 [24, 27, 28], which has excellent protective properties and can effectively make up for the loose and porous MgO film layer and isolate air to prevent further oxidation. In addition, a large number of studies have shown that in Mg–Gd–Y series alloys, protective oxide films such as Gd<sub>2</sub>O<sub>3</sub> and Y<sub>2</sub>O<sub>3</sub> can be formed at high temperatures to prevent the diffusion of oxygen elements and alloying elements, so they have excellent anti-oxidation properties [29–32]. The alloy studied in this article contains fewer Zr elements, and the number of Zr elements that can participate in film formation is limited. Therefore, the Gd and Y elements added simultaneously in the alloy play a significant role.

According to thermodynamic theory, the following reactions may occur during oxidation:



Under actual conditions, the Gibbs free energy of reaction formula (3–6) can be calculated as follows [24, 25, 29]:

$$\Delta G_{\text{MgO}} = \Delta G_{\text{MgO}}^\theta + RT \ln(\alpha_{\text{MgO}} \cdot \alpha_{\text{Mg}}^{-1} \cdot \alpha_{\text{O}_2}^{-1/2}). \quad (7)$$

$$\Delta G_{\text{Gd}_2\text{O}_3} = \Delta G_{\text{Gd}_2\text{O}_3}^\theta + RT \ln(\alpha_{\text{Gd}_2\text{O}_3}^{1/2} \cdot \alpha_{\text{Gd}}^{-1} \cdot \alpha_{\text{O}_2}^{-3/4}). \quad (8)$$

$$\Delta G_{\text{Y}_2\text{O}_3} = \Delta G_{\text{Y}_2\text{O}_3}^\theta + RT \ln(\alpha_{\text{Y}_2\text{O}_3} \cdot \alpha_{\text{Y}}^{-1} \cdot \alpha_{\text{O}_2}^{-3/4}). \quad (9)$$

$$\Delta G_{\text{ZrO}_2} = \Delta G_{\text{ZrO}_2}^\theta + RT \ln(\alpha_{\text{ZrO}_2} \cdot \alpha_{\text{Zr}}^{-1} \cdot \alpha_{\text{O}_2}^{-1}). \quad (10)$$

where  $\Delta G_{\text{MgO}}$ ,  $\Delta G_{\text{Gd}_2\text{O}_3}$ ,  $\Delta G_{\text{Y}_2\text{O}_3}$ , and  $\Delta G_{\text{ZrO}_2}$  are the reaction free energies under actual conditions, respectively,  $\Delta G_{\text{MgO}}^\theta$ ,  $\Delta G_{\text{Gd}_2\text{O}_3}^\theta$ ,  $\Delta G_{\text{Y}_2\text{O}_3}^\theta$ , and  $\Delta G_{\text{ZrO}_2}^\theta$  are the standard free energies of their reactions, respectively,  $\alpha_{\text{Mg}}$ ,  $\alpha_{\text{MgO}}$ ,  $\alpha_{\text{Gd}}$ ,  $\alpha_{\text{Gd}_2\text{O}_3}$ ,  $\alpha_{\text{Y}}$ ,  $\alpha_{\text{Y}_2\text{O}_3}$ ,  $\alpha_{\text{Zr}}$ , and  $\alpha_{\text{ZrO}_2}$  are the activities of Mg, MgO, Gd, Gd<sub>2</sub>O<sub>3</sub>, Y, Y<sub>2</sub>O<sub>3</sub>, Zr, and ZrO<sub>2</sub>, respectively.

By inputting thermodynamic data and the molar fractions of Mg, Gd, Y, and Zr in Mg–6.5Gd–5.6Y–0.1Nd–0.01Ce–0.4Zr–xAg alloy into formulas (7–10), it can be obtained that  $\Delta G$  value, as shown in Table 4. The numerical value of free energy represents the ease of forward reaction. The smaller the  $\Delta G$  value, the easier the reaction to occur. According to the above results, it can be concluded that between 623 K and 723 K, their reaction sequence is Y<sub>2</sub>O<sub>3</sub> > Gd<sub>2</sub>O<sub>3</sub> > ZrO<sub>2</sub> > MgO. Therefore, Gd, Y, and Zr elements are oxidized prior to Mg, and composite films such as Y<sub>2</sub>O<sub>3</sub>, Gd<sub>2</sub>O<sub>3</sub>, ZrO<sub>2</sub>, and MgO are detected on the surface, which protects the matrix.

As the oxidation temperature increases, the tensile stress on the surface of the oxide film increases, and stress concentration occurs, resulting in cracks. The oxidation process continues, and oxygen in the air diffuses into the matrix through the crack channels, causing many alloy elements in the matrix to diffuse to the surface to form the oxide film, making the oxide film gradually thicker. When a complete oxide film is formed again, it can regain the protective effect on the alloy. At this time, the oxidation rate is significantly reduced, and the oxidation proceeds slowly. The oxidation process is shown in Fig. 11. In addition, this article observed differences in the impact mechanism of Ag added to the alloy on the alloy at different temperatures, and further analysis was conducted.

## 4.2 Effect of Ag on the Diffusion of Alloy Elements

Experimental results show that the addition of Ag element can promote the formation of the alloy eutectic phase, resulting in a reduction in the content of Gd and Y elements in the matrix. At 350 °C and 400 °C, reducing the diffusion rate and making the formation of the oxide film slower than that of the 0Ag alloy, which leads to a more significant oxidation weight gain of the Ag-containing alloy. At this time, the addition of Ag hurts the oxidation resistance of the alloy. As shown in Fig. 12 and Table 5, under the condition of oxidation at 400 °C for 120 h, as the Ag content gradually increases, the total content of Gd and Y elements at P<sub>1</sub>–P<sub>4</sub> in the matrix gradually decreases,

**Table 4** Gibbs free energy of actual reactions at temperatures of 623 K, 673 K, and 723 K (J/mol)

Temperatures	$\Delta G_{\text{MgO}}$	$\Delta G_{\text{Gd}_2\text{O}_3}$	$\Delta G_{\text{Y}_2\text{O}_3}$	$\Delta G_{\text{ZrO}_2}$
623 K	–653,428.9	–1,969,362.0	–2,026,730.2	–1,196,767.3
673 K	–658,862.3	–1,984,915.0	–2,039,706.9	–1,142,166.5
723 K	–633,568.0	–2,000,984.9	–2,001,309.0	–1,147,496.5

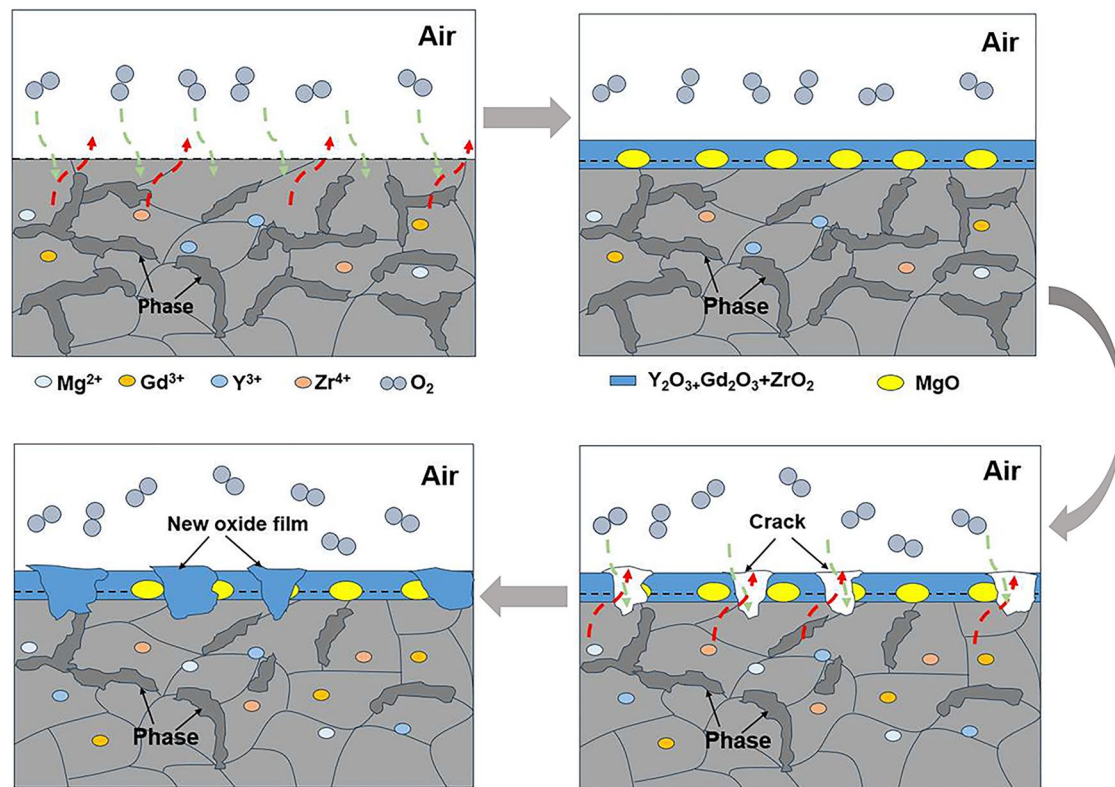


Fig. 11 Schematic diagram of the oxidation process

consistent with the previously inferred results. Moreover, the higher the element content in the matrix, the faster the element diffusion. The oxide film can be formed faster to prevent the further diffusion of O elements into the interior of the alloy matrix, reduce the oxidation rate, and restrain the progress of oxidation. This is also the main reason why 0Ag alloy has better oxidation resistance. Under oxidation at 400 °C for 120 h, the change pattern of Gd and Y element content at P<sub>5</sub>-P<sub>8</sub> in the matrix is the same as that at 350 °C, and they gradually decrease with the increase in Ag content. At this time, the oxidation resistance of 0Ag alloy is higher than that of Ag-containing alloy.

However, a large amount of the eutectic phases in the alloy dissolve at 450 °C. The content of Gd and Y elements at P<sub>9</sub>-P<sub>12</sub> in the matrix increases compared with that at 350 °C and 400 °C. The differences in the content of Gd and Y elements in each alloy are minor. The influence on the oxidation rate of the alloys is weakened. At this temperature, Ag significantly promotes the diffusion of Gd and Y elements, which is the main reason for the difference in oxidation rate. As shown in Fig. 13, the diffusion of each element at 350 °C and 400 °C is similar, and there is no noticeable difference. The content of alloy elements near the oxide film has slight fluctuations. This is because elements such as Gd, Y, Zr, and Mg can diffuse to the alloy surface

area and contact oxygen to form an oxide film. Judging from the curve, the oxidation reaction here is feeble. This may be because the oxidation temperature at 400 °C is relatively low, and the protective effect of the oxide film is very excellent, effectively preventing the oxidation from proceeding. In addition, no apparent effect of the Ag element on the diffusion of alloy elements is found during the oxidation process. However, the diffusion trends of each element are significantly different at 450 °C. Compared with 350 °C and 400 °C, the concentration of elements near the oxide film is significantly increased, and the degree of oxidation continues to increase, indicating that there are more elements such as Gd, Y, and Zr. It diffuses to the alloy surface area and reacts with O elements to form an oxide film to protect the matrix from further oxidation. This is mainly due to the increase in temperature, which leads to a more robust diffusion driving force of elements. The greater tensile stress on the oxide film causes rupture, allowing the oxidation reaction to continue, and a complete oxide film needs to be re-formed to protect the matrix.

At this time, it is observed that the addition of Ag element significantly promoted the diffusion of Gd and Y elements, which can quickly form protective oxide films such as Gd<sub>2</sub>O<sub>3</sub> and Y<sub>2</sub>O<sub>3</sub> on the alloy surface, effectively

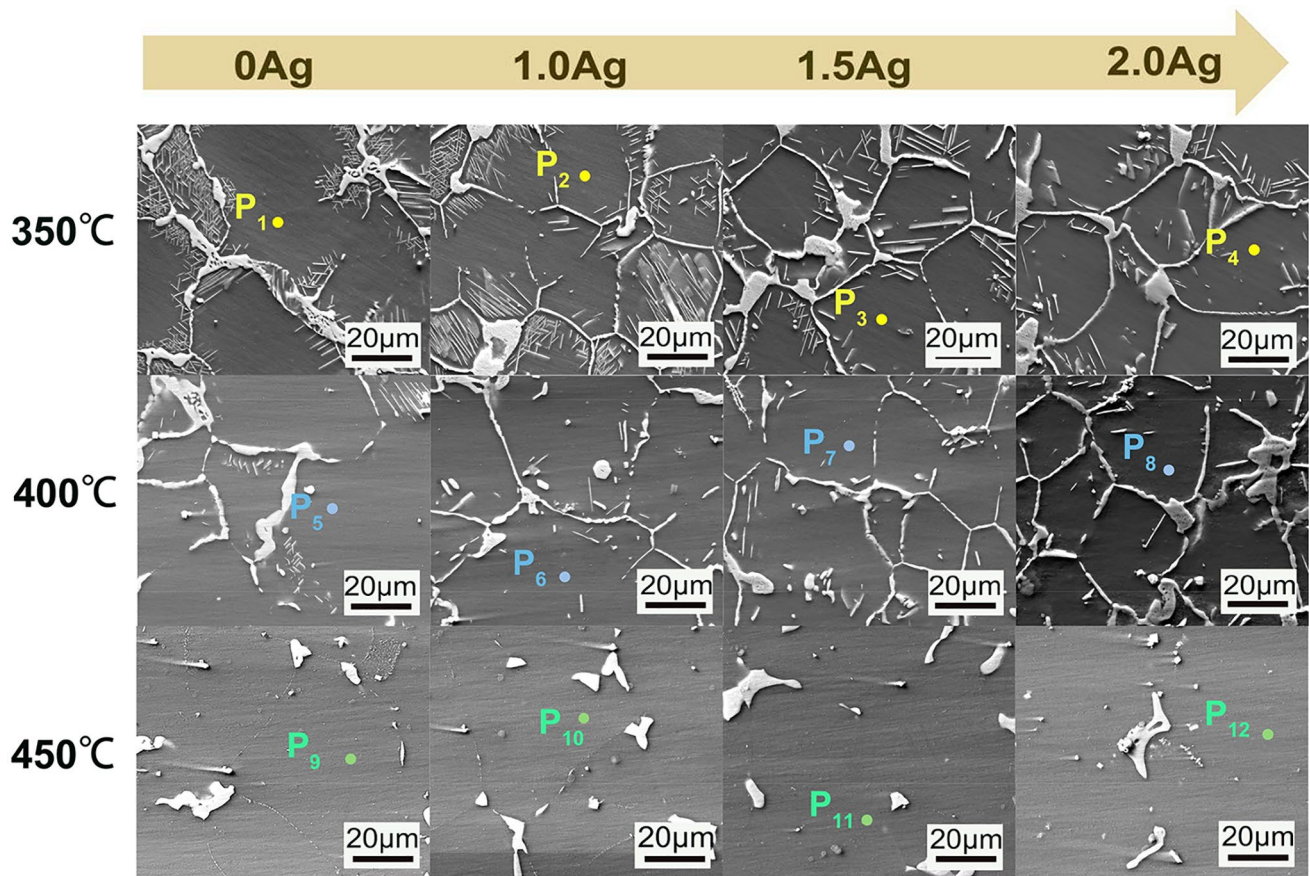


Fig. 12 Cross-sectional morphologies of four alloys oxidized for 120 h at different temperatures

**Table 5** EDS analysis of the matrix of four alloys oxidized for 120 h at different temperatures (wt%)

Points	Mg	Gd	Y
P <sub>1</sub>	92.49	3.47	4.04
P <sub>2</sub>	93.63	3.00	3.37
P <sub>3</sub>	94.43	2.77	2.80
P <sub>4</sub>	94.79	2.63	2.58
P <sub>5</sub>	90.89	4.96	4.16
P <sub>6</sub>	91.78	4.25	3.96
P <sub>7</sub>	92.54	3.89	3.57
P <sub>8</sub>	92.90	3.51	3.59
P <sub>9</sub>	88.59	6.36	5.05
P <sub>10</sub>	88.36	6.22	5.42
P <sub>11</sub>	89.02	5.34	5.64
P <sub>12</sub>	89.49	5.38	5.13

protecting the matrix and improving the oxidation resistance of the alloy. Among them, the diffusion effect of 1.0Ag alloy is the most significant, indicating that the effect is best when the amount of Ag added reaches 1.0%, and the oxidation difference at 450 °C can be explained by this.

## 5 Conclusions

This article systematically studied the effect of Ag on the high-temperature oxidation behavior of Mg–6.5Gd–5.6Y–0.1Nd–0.01Ce–0.4Zr alloy under the conditions of 350 °C, 400 °C, and 450 °C for 120 h. The main conclusions were as follows:

1. The oxidation weight gain of the four alloys after oxidation at 350 °C and 400 °C for 120 h approximately followed the law of logarithmic function curve. The 0Ag alloy had the best oxidation resistance. After oxidation at 450 °C for 120 h, the oxidation weight gain of the four alloys approximately followed the law of a quadratic exponential function curve. At this time, the 1.0Ag alloy had the best oxidation resistance.
2. The oxidation products produced by the four alloys after oxidation at different temperatures had the same phase types: MgO, Y<sub>2</sub>O<sub>3</sub>, Gd<sub>2</sub>O<sub>3</sub> and ZrO<sub>2</sub>. The thickness of the oxide film gradually increased as the temperature increased. There was no apparent boundary between the several oxidation products, and they were evenly distributed on the surface of the alloys.

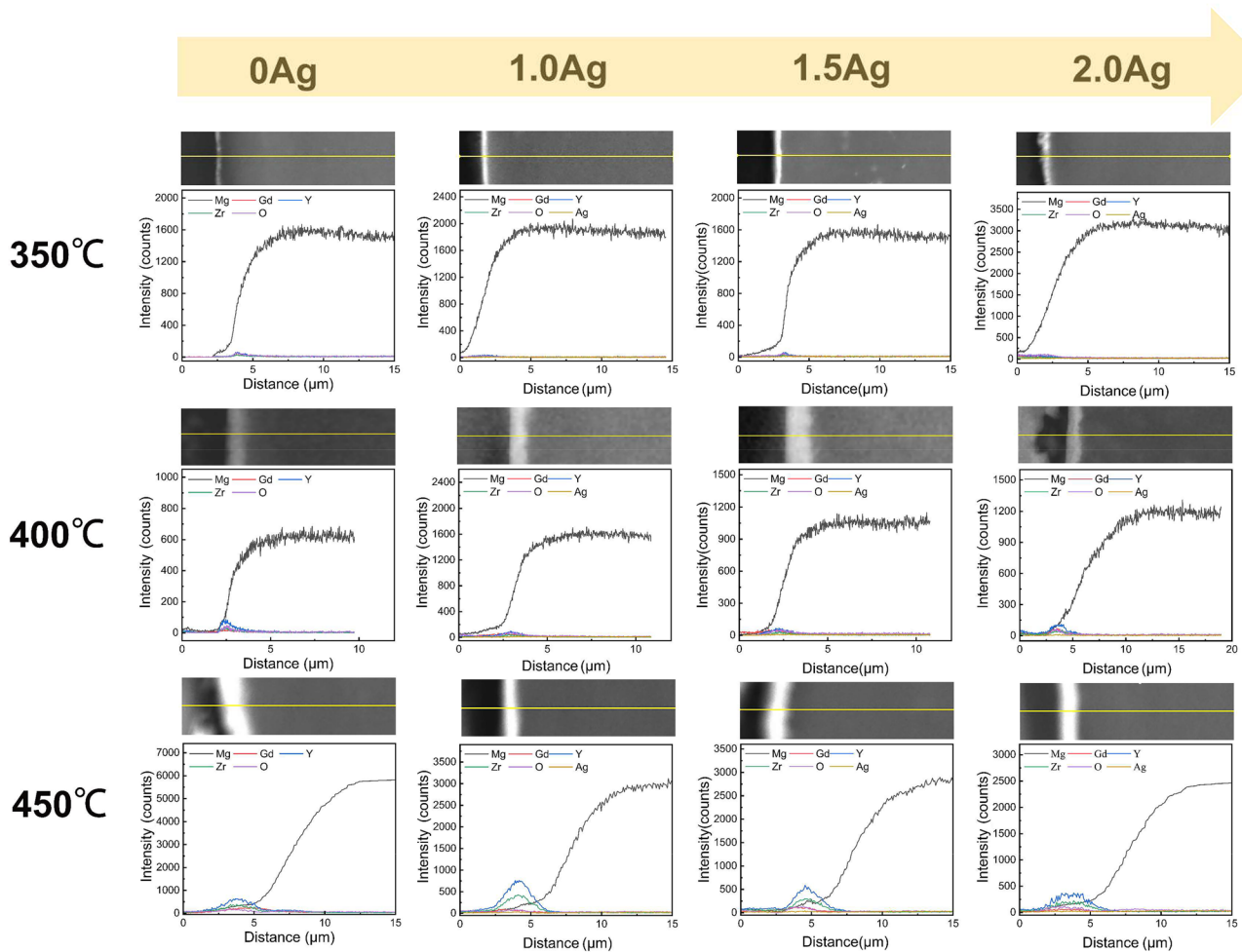


**Fig. 13** Microstructure cross-section scanning curves of four alloys oxidized for 120 h at different temperatures

3. The mechanism of the influence of the Ag element on the alloy oxidation process is different at different temperatures. When oxidation occurred at 350 °C and 400 °C, the proportion of the second phase increases with the increase in Ag content, resulting in a decrease in the content of Gd and Y elements in the alloy matrix, which reduced the oxidation resistance of the alloys. However, when the temperature rose to 450 °C, Ag can significantly promote the diffusion of Gd and Y elements, and improve the oxidation resistance of the alloys.

**Acknowledgements** This work was financially supported by the National Key Research and Development Program of China (No. 2021YFB3701100), the National Key Research and Development Program of China (No. 2016YFB0301105), the Applied Basic Research Program Project of Liaoning Province of China (No. 2023020253-JH2/1016), the Key Research and Development Plan of Shanxi Province (No. 202102050201005) and the Dongguan Innovative Research Team Program (No. 2020607134012).

## Declarations

**Conflict of interest** The authors state that there are no conflicts of interest to disclose.

## References

- [1] N.Y. Liu, Z.Y. Zhang, L.M. Peng, W.J. Ding, *Mater. Sci. Eng. A* **627**, 223 (2015)
- [2] J.J. Wang, A.B. Phillion, G.M. Lu, *J. Alloys Compd.* **609**, 290 (2014)
- [3] J.J. Wang, Z.M. Zhang, A.B. Phillion, S.Z. Shang, G.M. Lu, *J. Mater. Res.* **31**, 2482 (2016)
- [4] X.S. Xia, Q. Chen, Z.D. Zhao, M.L. Ma, X.G. Li, K. Zhang, *J. Alloys Compd.* **623**, 62 (2015)
- [5] B.L. Mordike, T. Ebert, *Mater. Sci. Eng. A* **302**, 37 (2001)
- [6] N.J. Kim, *Mater. Sci. Technol.* **30**, 1925 (2014)
- [7] W.F. Mo, L. Zhang, G.H. Wu, Y. Zhang, W.C. Liu, C.L. Wang, *Mater. Des.* **63**, 729 (2014)
- [8] J. Wang, J. Meng, D.P. Zhang, D.X. Tang, *Mater. Sci. Eng. A* **456**, 78 (2007)

- [9] H.R.J. Nodooshan, W.C. Liu, G.H. Wu, R. Alizadeh, R. Mahmudi, W.J. Ding, *J. Alloys Compd.* **619**, 826 (2015)
- [10] J.F. Nie, X. Gao, S.M. Zhu, *Scr. Mater.* **53**, 1049 (2005)
- [11] H.R.J. Nodooshan, W.C. Liu, G.H. Wu, Y. Rao, C.X. Zhou, S.P. He, W.J. Ding, R. Mahmudi, *Mater. Sci. Eng. A* **615**, 79 (2014)
- [12] S.M. He, X.Q. Zeng, L.M. Peng, X. Gao, J.F. Nie, W.J. Ding, *J. Alloys Compd.* **427**, 316 (2007)
- [13] J.N. Yu, W.D. Jian, B.Z. Xiao, *Acta Metall. Sin. -Engl. Lett.* **36**, 295 (2023)
- [14] K. Yamada, H. Hoshikawa, S. Maki, T. Ozaki, Y. Kuroki, S. Kamadoa, Y. Kojimaa, *Scr. Mater.* **61**, 636 (2009)
- [15] L.M. Peng, J.W. Chang, X.W. Guo, A. Atrens, W.J. Ding, Y.H. Peng, *J. Appl. Electrochem.* **39**, 913 (2009)
- [16] Y. Zhang, Y.J. Wu, L.M. Peng, P.H. Fu, F. Huang, W.J. Ding, *J. Alloys Compd.* **615**, 703 (2014)
- [17] X. Gao, J.F. Nie, *Scr. Mater.* **58**, 619 (2008)
- [18] H. Zhou, Q.D. Wang, J. Chen, B. Ye, W. Guo, *Trans. Nonferrous Met. Soc.* **22**, 1891 (2012)
- [19] Y. Zhang, T. Alam, B. Gwalani, W. Rong, R. Banerjee, L.M. Peng, *Phil. Mag. Lett.* **96**, 212 (2016)
- [20] S. Najafi, R. Mahmudi, *J. Magnes. Alloy.* **8**, 1109 (2020)
- [21] Y. Chen, J.C. Pang, S.X. Li, Z.F. Zhang, *Acta Metall. Sin. -Engl. Lett.* **35**, 1117 (2022)
- [22] Y. Yang, L. Peng, P. Fu, B. Hu, W. Ding, *J. Alloys Compd.* **485**, 245 (2009)
- [23] J.X. Zheng, Z.Y. Luo, L. Tan, B. Chen, *Microsc. Microanal.* **22**, 1244 (2016)
- [24] J. Askill, *Tracer diffusion data for metals, alloys, and simple oxides* (Springer, Berlin, 2012)
- [25] L. Wu, Z. Yang, *J. Alloys Compd.* **626**, 194 (2015)
- [26] F. Czerwinski, *JOM* **64**, 1477 (2012)
- [27] Q.Y. Tan, A. Atrens, N. Mo, M.X. Zhang, *Corros. Sci.* **112**, 734 (2016)
- [28] D.J. Young, *High-temperature oxidation and corrosion of metals* (Elsevier, New York, 2008)
- [29] X.M. Wang, W.D. Wu, Y.J. Tang, X.Q. Zeng, S.S. Yao, *J. Alloys Compd.* **474**, 499 (2009)
- [30] J.W. Liu, Y. Li, F.H. Wang, *Oxid. Met.* **71**, 319 (2009)
- [31] X.W. Yu, B. Jiang, J.J. He, B. Liu, F.S. Pan, *J. Alloys Compd.* **749**, 1054 (2018)
- [32] J.F. Fan, C.H.L. Yang, G. Han, S. Fang, W.D. Yang, B.S. Xu, *J. Alloys Compd.* **509**, 2137 (2011)

Springer Nature or its licensor (e.g. a society or other partner) holds exclusive rights to this article under a publishing agreement with the author(s) or other rightsholder(s); author self-archiving of the accepted manuscript version of this article is solely governed by the terms of such publishing agreement and applicable law.